Development of a Wearable Robotic Positioning System for Noninvasive Transcranial Focused Ultrasound Stimulation

Junwoo Kim and Sungon Lee, *Member, IEEE*

Abstract—**Transcranial ultrasound neuromodulation has been attracting more and more interest from researchers as a novel modality for brain stimulation. Typical manual positioning for brain stimulation requires the patient to sit still during stimulation for extended periods and readily loses its positioning accuracy if the patient moves. To address these problems of inconvenience and inaccuracy, we proposed a robotic positioning system for targeted ultrasound brain stimulation. The proposed device automatically moves the ultrasound transducer to a desired position and orientation, enabling far more accurate and comfortable automatic positioning of the transducer than when using traditional manual positioning. The device was developed as a wearable design because it eliminates the necessity for troublesome motion compensation for the user's unintentional movements. Parallel and serial mechanisms were combined and a torque optimization method was proposed so as to obtain a lightweight design and to implement a sufficient number of degrees of freedom of motion.**

Index Terms—**Noninvasive brain stimulation and treatment, robotic positioning system, transcranial magnetic stimulation, and ultrasound stimulation.**

I. INTRODUCTION

NONINVASIVE brain stimulation has become an important method in research and therapeutic applications [1]. For example, transcranial magnetic stimulation (TMS) has been approved by the U.S. Food and Drug Administration (FDA) for use in treating migraine and treatment-resistant major depressive disorder; it is now being used in clinical practice. Compared to invasive treatments, noninvasive stimulation has significant advantages such as being free of surgical procedures and having relatively few adverse effects.

There are several noninvasive stimulation methods. Transcranial direct current stimulation (tDCS) and TMS are two representative noninvasive brain stimulation methods. To modulate brain function, tDCS polarizes brain regions by applying weak direct currents, whereas TMS induces electrical currents at the stimulated sites by applying a short, strong magnetic field using a magnetic coil. Recently, ultrasonic brain stimulation has emerged as a novel noninvasive brain stimulation modality showing improved penetration and spatial resolution over existing noninvasive brain stimulation methods. Not only animal experiments but also recent experiments on human subjects have shown the promising capabilities of ultrasound as a novel neuro-modulation modality [2-9].

Historically, ultrasound has been studied by many researchers. Fry et al. showed reversible suppression of visual evoked potentials without observable damage [10]. Mihran et al. have shown that ultrasound can modulate neuronal activity through either enhancement or suppression of its excitability in peripheral nerves [11]. Recently, multiple researchers were successful in inducing observable selective motor activities by stimulating the intact brains of mice [5-7]; one of these groups recently conducted extended experiments on human subjects, showing that ultrasound can focally modulate human cortical function [2].

Ultrasonic noninvasive brain stimulation can offer improved brain stimulation: it has better spatial resolution and deeper penetration than traditional noninvasive methods such as tDCS and TMS. Although there have been many animal experiments regarding ultrasound's effect on brain stimulation, investigation on the human brain is still in its infancy. More scientific studies to investigate ultrasound effects on the human brain should be conducted. To conduct these experiments, first, ultrasound transducers should be located at the desired locations on the head. Therefore, it is very important to have an accurate positioning system to allow precise and repetitive stimulation. For example, in typical TMS experiments, a TMS coil is placed on the subject's head with a rigid mechanical arm holding the coil. Subjects are asked to keep their head as still as possible. In this manual setup, it is not easy to move the coil accurately and precisely; furthermore, the stimulated point will easily change as the subject unintentionally moves during stimulation. Head fixation (e.g., using a chin rest) is a short-term solution [12]; however, it is not desirable because it can cause serious discomfort to the patient, particularly during prolonged treatments. For instance, one treatment session of repetitive transcranial magnetic stimulation typically lasts up to 30 min [13].

J. Kim is with the Korea Polar Research Institute, 26 Sondomirae-ro, Yeonsu-gu, Incheon 406-840 Republic of Korea (e-mail: kimjunwoo@gmail.com). S. Lee, was with the School of Electrical Engineering, Hanyang University, 55 Hanyangdaehak-ro, Sangnok-gu, Ansan, 426-791 Republic of Korea (e-mail: sungon@hanyang.ac.kr).
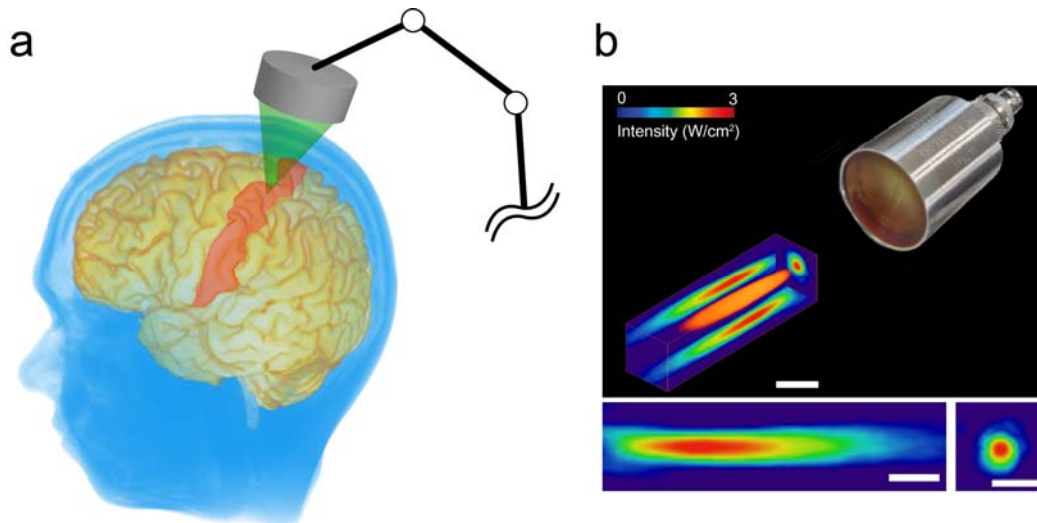
Figure 1. Transcranial focused ultrasound stimulation (FUS). (a) Concept of brain stimulation by FUS. (b) A single-element focused ultrasound transducer and its three-dimensional ultrasound intensity map. Scale bar 1cm.

Therefore, an active positioning system will make the essential positioning task accurate and easy. Furthermore the subject's movement does not need to be constrained during treatment. As a result, brain stimulation experimental procedures with the active positioning system will be far more accurate, rapid, convenient, and safe. Data from these experiments will be more reliable than that of manual positioning. Additionally, sophisticated experiments can be designed such as brain mapping for small areas. Based on these advantages, researchers using TMS have started to use a robot-assisted stimulation system [13]. It has been shown that robotic positioning significantly improves the stimulation accuracy compared to conventional manual positioning. Because transcranial ultrasound stimulation has spatial resolution of 3~5 mm which is better than that of transcranial magnetic stimulation which is ~ 1cm [2-3], it is reasonable to expect that the automatic positioning system will have a stronger effect on the results of experiments. In addition, safety is an important issue in an autonomous system interacting with subjects. For this reason, although it would be possible to use a commercial, general-purpose serial robotic arm as a positioning system, it would be far better to develop a task-specific robotic system that highly weights safety, because the serial robotic arm could strike and damage the subject if the control fails. Taking into account human head geometry, Zorn et al. proposed a specially designed robotic system for TMS [14]. They designed the robot arm to have spherical linkages, limiting the high inertial motion to the direction tangential to the subject's head. This robot can be used for positioning for ultrasound brain stimulation although this is a huge system (~400 Kg) and the subject should stay seated on a chair.

Although it is not for brain stimulation, some robots have been developed for ultrasound imaging probe positioning [15-17]. A robot being based on parallelogram linkage was firstly proposed to position ultrasound probes [15]. This system has proposed various features such as ultrasound image based visual servoing. This robot has full six degrees of freedom (DOF) and large workspace. A small sized three DOF and four DOF robots were proposed for manipulating endocavity ultrasound probe [16]. They applied it to radical prostatectomy operation enabling the surgeon to observe ultrasound images intraoperatively. The robot is small and light weighted. But, it cannot be applied to our brain stimulation because its workspace is totally different from our target workspace. Recently, a minimal robot was proposed for immobilizing the ultrasound probe position which is manually determined in advance by the surgeon [17]. This robot is a passive arm with automatic brake system. The proposed minimal design makes the robot very simple and light weighted. This can be a good working solution when accuracy level of manual positioning is sufficient for its purpose and target position does not change frequently.

In this paper, we describe our development of an ultrasound brain stimulation robotic device. We developed this device with a wearable design because such designs have many advantages. First, there is no need for head motion compensation because the device is fixed to the user's head and moves with the user. Unintentional motion is one of main sources of error in medical devices, and thus, must be addressed for precise control [18]. Second, the wearable device minimally constrains the user's movement, thus enabling various experiments (e.g., subjects can walk during stimulation). Currently, the subject must sit on a chair to undergo brain stimulation.

Parallel design of the linkage and optimization of the linkage parameters resulted in a wearable size and weight for the device. For wearable design in which optimized design and consideration of human-body geometry are needed, parallel mechanisms are good candidates [19]. The wearable robotic device consists of two modules: a two-degrees-of-freedom (DOF) parallel spherical five-bar linkage and a three-DOF serial arm, implementing five-DOF motion on a human head. The parallel component locates the stimulator around the
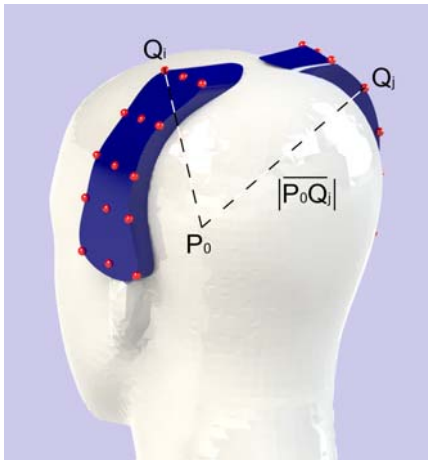
Figure 2. Desired workspace (blue region) of the FUS stimulation device including somatosensory strip in the human brain responsible for arm, hand and face, and selection of design points. Red spheres represent the selected design points Q_i ($i = 1, …, 30$)

human head, and the serial component controls the stimulation angle and depth. The workspace of this robot includes all positions that allow stimulation of the postcentral gyrus, a region in the primary somatosensory cortex in the left and right brain. This target workspace was chosen for future studies of the ultrasound effect on the activity of the primary somatosensory cortex.

One of the potential applications of the developed device is to use it for a study on the modulation of the activity of the primary somatosensory cortex in human as in the reference [2, 4]. Especially, we are interested in selectively stimulating the hand/arm subdivision in somatotopic map. Functional MRI studies of human somatotopic map of hand showed that the activation area (thumb to little finger) spans ~18 mm and the interdigit distances vary from ~3 to ~6 mm [20]. To provide sufficient accuracy in those target experiments, the device should have at least far less than 3 mm accuracy. Our design goal was, therefore, set to have submillimeter accuracy.

This paper is organized as follows: The desired specifications and an overview of the device are presented in Section II. Forward and inverse analysis of the device and the optimal design methods for the spherical parallel manipulator are given in Section III. In Section IV, the experimental results for the prototype are described. Finally, conclusions are given in Section V.

II. Brain Stimulation using Ultrasound

This research proposes a new robotic device that stimulates the brain cortices using noninvasive ultrasound through the skull, as depicted in Fig. 1(a). Ultrasound is expected to be a novel noninvasive brain stimulation modality with improved spatial resolution and penetration compared to the existing modalities using electricity, as in tDCS, and magnetic fields, as in TMS.

A. Ultrasound Stimulation

Recently, it was shown that ultrasound can modulate the activity of the human brain [2, 4]. Previously, it has been widely proven by many researchers that ultrasound can elicit neural activities and behavioral effects in intact animal brains.

Ultrasound brain stimulation is performed using an ultrasound transducer. The ultrasound transducer is a device that converts electrical energy into acoustic energy. The intensity of ultrasound is proportional to the sound pressure. Ultrasound can be focused using either an acoustic lens or a curved transducer. Fig. 1(b) shows an example of a single-element, focused ultrasound transducer using an acoustic lens and its three-dimensional acoustic intensity map. This intensity map was drawn after experimentally obtaining intensity data from three-dimensional sampling points in the region of interest. The intensity value is obtained using a hydrophone to measure the pressure. The colored intensity map shows the typical shape of single-element, focused ultrasounds. The focal area is characterized by the focal region, which is defined as the volume of the beam in which the acoustic intensity is within 3 dB of the maximum value. Due to the existence of the skull absorbing and refracting ultrasound, a low frequency ultrasound, typically less than 1 MHz, has been adopted in the transcranial applications [21]. In the Fig.1 (b) where the measurement with a 500 KHz focused ultrasound was performed, the focal size was 5 mm in the lateral and 40 mm in the axial directions of sonication. Generally, the focal region of the focused ultrasound is an ellipsoid with a longer semi-major axis along the line of the stimulation beam than along the line perpendicular to the beam.

In this study, the targeted stimulation region in the brain was determined to include the left and right primary somatosensory cortices of a human brain. We chose this targeted stimulation area because our future neuroscience work is to investigate the ultrasound effects on the activity of the primary somatosensory cortex in a human brain. This region is known to be responsible for the processing of tactile information [22]. This region in the brain is highlighted in red in Fig. 1(a). The primary somatosensory area in the right or left brain is a long, narrow band (Fig. 2). The workspace of the robotic positioning system not only needs to include both primary somatosensory cortices, but also needs to be sufficiently larger than this to be able to adapt to diverse sizes and shapes of people's heads. The desired workspace was determined based on anthropometric data on Korean males between 20 and 50 years old [23].

B. Automatic Positioning of Ultrasound Transducer

Precise positioning of the ultrasound transducer is critical to the success of targeted brain stimulation. An automatic robotic positioning system is designed by considering the target workspace and task specifications, which are described in the previous section. This robotic device consists of two

submodules. One is a two-DOF spherical parallel mechanism (hereafter, SPM) and the other is a three-DOF serial revolute-revolute-prismatic mechanism (hereafter, RRP). RRP is serially connected to one link of the SPM; the ultrasound transducer is mounted on the prismatic actuator of RRP, as shown in Fig. 3. The spherical mechanism enables a compact design covering a spherical-shaped workspace around the human head using a simple structure. Although a serial spherical 2R (revolute-revolute) manipulator can be another candidate for spherical submodule, we decided to use SPM because of high stiffness, high accuracy and low inertia characteristics of its parallel architecture [24-25]. Finally, the second submodule, RRP, determines the direction and the depth of stimulation. The three joints of RRP intersect at the center point, as shown in Fig. 3.

III. DESIGN OF MECHANISM

In this research, the SPM was determined to be symmetrical because of the left-right-symmetric geometry of the target workspace. Symmetric SPM has four working modes based on the configurations of left and right arms, as shown in Fig. 4. Here, the first mode [the down-up mode, which is depicted in Fig. 4(a)] was selected and used for design because of its large workspace [26-27].

The proposed device is designed such that the instantaneous motion systems of SPM and RRP can be decomposed to allow simple design and analysis. To achieve this decomposition, three actuators of RRP are designed such that two axes of the rotational actuators and the line of translation of the prismatic actuator meet at the point, as shown in Fig. 3. Because of this design constraint, the distance between the centers of SPM and RRP becomes constant during the operation. Then, the instantaneous motion of SPM (or RRP) can be represented by the twist axis that passes the center of SPM (or RRP).

Based on the determination mentioned above, the proposed device can be modeled as shown in Fig. 3. The constant distance r between centers of SPM ($P0$) and RRP ($P3$) can be written as

$$r = \sqrt{d_1^2 + d_2^2} \qquad (1)$$

Although the ideal decomposition can be achieved when d_2 is zero, here, d_2 was designed to be nonzero because of the space required for mechanical elements.

A. Forward Position Analysis

Consider the coordinate frames F_k ($k = 0, ..., 6$) that have their origins at P_k. When the input values of the five actuators (two for SPM and three for RRP) are $\theta_1, \theta_2, \theta_3, \theta_4,$ and d, the transformation matrices $\mathbf{A}_{ij} \in R^{4 \times 4}$ ($i = 0,...,5,$ and $j = 1, ..., 6$) relating two successive coordinate systems F_i and F_j can be written as
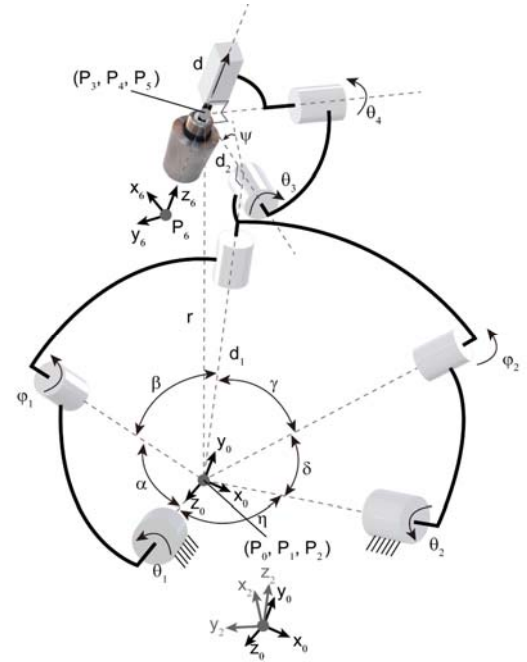

Figure 3. Schematic diagram of the proposed device. $\theta_{1\sim4}$ and d are active joint variables, whereas $\varphi_{1,2}$ are passive joint variables. α, β, γ, δ, and η are variables of linkage length to be determined by the proposed optimization.

$$\mathbf{A}_{01} = \begin{bmatrix} c_{\theta_1} & -s_{\theta_1} & 0 & 0 \\ s_{\theta_1} & c_{\theta_1} & 0 & 0 \\ 0 & 0 & 1 & 0 \\ 0 & 0 & 0 & 1 \end{bmatrix} \begin{bmatrix} c_\alpha & 0 & s_\alpha & 0 \\ 0 & 1 & 0 & 0 \\ -s_\alpha & 0 & c_\alpha & 0 \\ 0 & 0 & 0 & 1 \end{bmatrix}, \qquad (2)$$

$$\mathbf{A}_{12} = \begin{bmatrix} c_{\varphi_1} & -s_{\varphi_1} & 0 & 0 \\ s_{\varphi_1} & c_{\varphi_1} & 0 & 0 \\ 0 & 0 & 1 & 0 \\ 0 & 0 & 0 & 1 \end{bmatrix} \begin{bmatrix} c_\beta & 0 & s_\beta & 0 \\ 0 & 1 & 0 & 0 \\ -s_\beta & 0 & c_\beta & 0 \\ 0 & 0 & 0 & 1 \end{bmatrix}, \qquad (3)$$

$$\mathbf{A}_{23} = \begin{bmatrix} 1 & 0 & 0 & 0 \\ 0 & 1 & 0 & 0 \\ 0 & 0 & 1 & d_1 \\ 0 & 0 & 0 & 1 \end{bmatrix} \begin{bmatrix} c_\psi & -s_\psi & 0 & 0 \\ s_\psi & c_\psi & 0 & 0 \\ 0 & 0 & 1 & 0 \\ 0 & 0 & 0 & 1 \end{bmatrix} \begin{bmatrix} 1 & 0 & 0 & d_2 \\ 0 & 1 & 0 & 0 \\ 0 & 0 & 1 & 0 \\ 0 & 0 & 0 & 1 \end{bmatrix}, \qquad (4)$$

$$\mathbf{A}_{34} = \begin{bmatrix} 1 & 0 & 0 & 0 \\ 0 & c_{\theta_3} & -s_{\theta_3} & 0 \\ 0 & s_{\theta_3} & c_{\theta_3} & 0 \\ 0 & 0 & 0 & 1 \end{bmatrix}, \qquad (5)$$
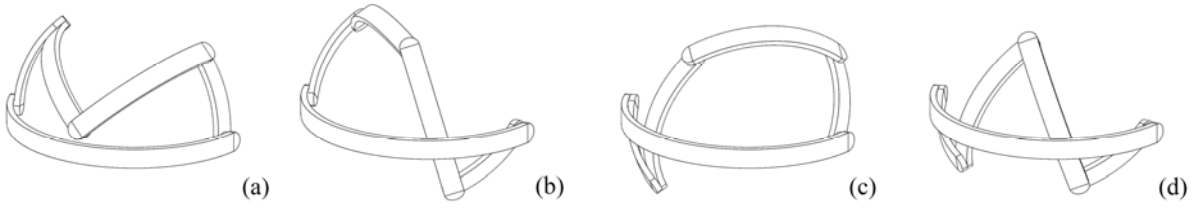
Figure 4. Four working modes of symmetric SPM. (a) down-up, (b) down-down, (c) up-up, (d) up-down modes.

$$\mathbf{A}_{45} = \begin{bmatrix} c_{\theta_4} & 0 & s_{\theta_4} & 0 \\ 0 & 1 & 0 & 0 \\ -s_{\theta_4} & 0 & c_{\theta_4} & 0 \\ 0 & 0 & 0 & 1 \end{bmatrix}, \tag{6}$$

$$\mathbf{A}_{56} = \begin{bmatrix} 1 & 0 & 0 & 0 \\ 0 & 1 & 0 & 0 \\ 0 & 0 & 1 & -d \\ 0 & 0 & 0 & 1 \end{bmatrix}, \tag{7}$$

where α and β are the angular lengths of the first and second links of SPM, ψ is a mounting angle of RRP with respect to SPM. When γ, δ, and η are the angular lengths of the third, fourth, and ground links as shown in Fig. 3, the rotation angle φ_1 in Eq. (3) can be obtained from the kinematic analysis of SPM as [26]

$$\varphi_1(\theta_1, \theta_2) = \arctan\left(\frac{Q}{P}\right) \pm \arccos\left(\frac{R}{\sqrt{P^2 + Q^2}}\right), \tag{8}$$

where

$$P = s_\beta \begin{pmatrix} c_\delta(-c_\eta s_\alpha + c_\alpha c_{\theta_1} s_\eta) \\ + s_\delta\left(c_{\theta_2}(c_\alpha c_\eta c_{\theta_1} + s_\alpha s_\eta) + c_\alpha s_{\theta_1} s_{\theta_2}\right) \end{pmatrix},$$

$$Q = s_\beta\left(c_{\theta_1} s_{\theta_2} s_\delta - s_{\theta_1}(c_\eta c_{\theta_2} s_\delta + c_\delta s_\eta)\right),$$

$$R = \left(c_\gamma - c_\beta\begin{pmatrix} c_\alpha(c_\delta c_\eta - c_{\theta_2} s_\delta s_\eta) \\ + s_\alpha\left(c_{\theta_1}(c_\eta c_{\theta_2} s_\delta + c_\delta s_\eta) + s_\delta s_{\theta_1} s_{\theta_2}\right) \end{pmatrix}\right),$$

c_θ and s_θ are used for $\cos\theta$ and $\sin\theta$. In Eq. (8), the angular lengths of the right leg of SPM can be written as $\gamma = \beta$ and $\delta = \alpha$ because the designed SPM is symmetrical. The signs ($\pm$) in Eq. (8) corresponds to the arm-up and arm-down configurations, respectively. The positive sign is selected here because the proposed device uses the first mode. From Eqs. (2)-(7), the transformation matrix $\mathbf{A}_{06}$, which relates the first coordinate system F_0 to the final one F_6 can be obtained as

$$\mathbf{A}_{06} = \mathbf{A}_{01}\mathbf{A}_{12}\mathbf{A}_{23}\mathbf{A}_{34}\mathbf{A}_{45}\mathbf{A}_{56} = \begin{bmatrix} u_x & v_x & w_x & p_x \\ u_y & v_y & w_y & p_y \\ u_z & v_z & w_z & p_z \\ 0 & 0 & 0 & 1 \end{bmatrix} \tag{9}$$

where $[u_x\ u_y\ u_z]^T$, $[v_x\ v_y\ v_z]^T$, and $[w_x\ w_y\ w_z]^T$ are the three unit vectors of coordinate axes of F_6 expressed in F_0 and $[p_x\ p_y\ p_z]^T$ represents the position vector from P_0 to P_6. Therefore, each of the position vectors $\boldsymbol{p}$ of the focal point and the direction vectors $\boldsymbol{s}$ expressed in F_0 are $\boldsymbol{p} = [p_x\ p_y\ p_z]^T$ and $\boldsymbol{s} = [w_x\ w_y\ w_z]^T$, respectively.

B. Inverse Position Analysis of Device

Let the desired direction cosine vector of the line of stimulation (LoS) and position vector of focal point be given by $\boldsymbol{s}_d$ and $\boldsymbol{p}_d$. As mentioned in Section II, the inverse position analysis of the proposed device can easily be conducted because of the decomposition of SPM and RRP. To progress the analysis, $\boldsymbol{p}_3$, which is the position vector from P_0 to P_3 should first be obtained. Because P_3 is a point on the LoS and the length of $\boldsymbol{p}_3$ is r, $\boldsymbol{p}_3$ should satisfy the following equations:

$$\boldsymbol{p}_3 = t\boldsymbol{s}_d + \boldsymbol{p}_d, \tag{10}$$

$$\boldsymbol{p}_3^T \boldsymbol{p}_3 = r^2, \tag{11}$$

where t is a parameter. Solving Eq. (10) and (11) simultaneously gives

$$t = -\boldsymbol{p}_d^T \boldsymbol{s}_d \pm \sqrt{(\boldsymbol{p}_d^T \boldsymbol{s}_d)^2 + (r^2 - \boldsymbol{p}_d^T \boldsymbol{p}_d)}. \tag{12}$$

If $\boldsymbol{s}_d$ is given such that $\boldsymbol{s}_d$ points from P_3 to P_6, t should have a negative value, which corresponds to the negative sign for the plus-minus sign ($\pm$) in Eq. (12). Substituting the obtained value of t into Eq. (10) yields the position of P_3. Now, the inverse position analysis can be regarded as two independent inverse position analyses of SPM and RRP for given value of P_6 and an obtained value of P_3.

1) Inverse position analysis of SPM for the obtained value of P_3

From Eqs. (2)-(4), the following relation can be obtained:

$$\mathbf{A}_{03}[0 \quad 0 \quad 0 \quad 1]^T = \boldsymbol{p}_3. \tag{13}$$

Solving Eq. (13) yields θ_1 and φ_1 for the first mode we consider as follows

$$\theta_1 = \arctan\left(\frac{-a_2 p_{3x} + a_1 p_{3y}}{a_1 p_{3x} + a_2 p_{3y}}\right), \tag{14}$$

$$\varphi_1 = \arctan\left(\frac{a_4(p_{3z} - a_5) + a_3\sqrt{a_3^2 + a_4^2 - (a_5 - p_{3z})^2}}{a_3(p_{3z} - a_5) - a_4\sqrt{a_3^2 + a_4^2 - (a_5 - p_{3z})^2}}\right), \tag{15}$$

where

$$c_{\theta_1} = \frac{a_1 p_{3x} + a_2 p_{3y}}{a_1^2 + a_2^2}, \quad s_{\theta_1} = \frac{-a_2 p_{3x} + a_1 p_{3y}}{a_1^2 + a_2^2},$$

$$a_1 = (c_\alpha s_\beta d_1 + c_\alpha c_\beta c_\psi d_2)c_{\phi_1} - (c_\alpha s_\psi d_2)s_{\phi_1} + (c_\beta s_\alpha d_1 - c_\psi s_\alpha s_\beta d_2),$$

$$a_2 = (s_\psi d_2)c_{\varphi_1} + (s_\beta d_1 + c_\beta c_\psi d_2)s_{\varphi_1},$$

$$a_3 = -s_\alpha s_\beta d_1 - c_\beta c_\psi s_\alpha d_2,$$

$$a_4 = s_\alpha s_\psi d_2,$$

$$a_5 = c_\alpha c_\beta d_1 - c_\alpha c_\psi s_\beta d_2,$$

and p_{3k} ($k = x, y, z$) represent the x, y, and z components of $\boldsymbol{p}_3$.

From the obtained values of θ_1 and φ_1, the coordinates n_x, n_y and n_z of the z-axis of F_2 expressed in F_0 can be calculated by

$$[n_x \quad n_y \quad n_z \quad 0]^T = \mathbf{A}_{02}[0 \quad 0 \quad 1 \quad 0]^T. \tag{16}$$

From the kinematic analysis of SPM [26], the input angle θ_2 for the right leg of SPM can be obtained as

$$\theta_2 = \arctan\left(\frac{b_1 n_y - b_2(c_\eta n_x - s_\eta n_z)}{b_1(c_\eta n_x - s_\eta n_z) + b_2 n_y}\right), \tag{17}$$

where

$$b_1 = \frac{1}{s_\alpha}\left(c_\beta - c_\alpha(n_x s_\eta + n_z c_\eta)\right),$$

$$b_2 = \sqrt{n_y^2 + (n_x c_\eta - n_z s_\eta)^2 - b_1^2}.$$

2) Inverse position analysis of RRP for the given value of P_6

Because the transformation matrix $\mathbf{A}_{03}$ is determined by the analysis of SPM, the equation for finding the last three input values (θ_3, θ_4, and d) of RRP can be written as

$$\mathbf{A}_{36}[0 \quad 0 \quad 0 \quad 1]^T$$
$$= \mathbf{A}_{03}^{-1}[p_{6x} \quad p_{6y} \quad p_{6z} \quad 1]^T \cdot \tag{18}$$
$$= [p'_{6x} \quad p'_{6y} \quad p'_{6z} \quad 1]^T$$

Equation (18) can be rewritten by

$$-d\, s_{\theta_4} = p'_{6x}, \tag{19}$$

$$d\, s_{\theta_3} c_{\theta_4} = p'_{6y}, \tag{20}$$

$$-d\, c_{\theta_3} c_{\theta_4} = p'_{6z}. \tag{21}$$

Solving Eqs. (19)-(21) simultaneously yields the input value d of the prismatic actuator as

$$d = \sqrt{p'^2_{6x} + p'^2_{6y} + p'^2_{6z}}. \tag{22}$$

By substituting Eq. (22) into Eqs. (19)-(21), the input angles θ_3 and θ_4 can be obtained by

$$\theta_3 = \arctan\left(-\frac{p'_{6y}}{p'_{6z}}\right), \tag{23}$$

$$\theta_4 = \arctan\left(-\frac{p'_{6x}}{\sqrt{p'_{6y} + p'_{6z}}}\right). \tag{24}$$

C. Design Optimization of SPM

SPM should be carefully designed to ensure the compactness of the proposed device. The total size and weight of the proposed device are mainly dependent on the sizes of actuators and the links of SPM. Furthermore, because the needed operating ranges of the actuators of RRP mechanism are affected by SPM, the size of the RRP mechanism is also dependent on the SPM. In this subsection, the design method of SPM to ensure the compactness of the device is presented.

The first step for achieving a compact design is to determine a suitable origin for SPM (P_0), at which all of the joint axes of SPM meet. First, the target design points on the target workspace should be selected such that they cover the workspace evenly. In total, thirty design points Q_i ($i = 1, …, 30$) on the surface of the workspace were selected here, as shown in Fig. 2; in general, these Q_i values are not on a common sphere. Unlike typical SPM, as used for orienting tasks, determining the position of P_0 is important when the SPM is used as part of a system that is performing positioning tasks. If P_0 is determined incorrectly, the deviation of distances ($|P_0Q_i|$) becomes large. Large deviations of $|P_0Q_i|$ lead to the need for a large range of motion of the other parts of the system. For the system considered here, a large deviation of $|P_0Q_i|$ values increases the size of RRP. From this reason, in this study, the origin P_0 was determined using a numerical method such that the standard

deviation of the distances $|P_0Q_i|$ is minimized. Based on the determination of P_0 using the above method, the deviation of distances between the transducer and the head can be kept small for every point in the target workspace.

The angular lengths of links of SPM were determined using an optimization method for maximizing the moment transmissibility so as to minimize the weights of the actuators. At a certain configuration of SPM, the optimization problem is to obtain a larger output moment with small input torques, which can be written as

$$maximize \quad \boldsymbol{m}^T\boldsymbol{m} = \boldsymbol{\tau}^T J_q^{-1} J_x J_x^T J_q^{-1} \boldsymbol{\tau} , \quad (25)$$

$$subject \ to \ \ \boldsymbol{\tau}^T \boldsymbol{\tau} = 1,$$

where $\boldsymbol{m}$ is the output moment vector, $\boldsymbol{\tau}$ is the input torque vector, and J_q and J_x are the Jacobian matrices of the parallel manipulator [28]. Equation (25) can be expressed as an eigenvalue problem using the Lagrange multiplier method as

$$J_q^{-1} J_x J_x^T J_q^{-1} \boldsymbol{\tau} = \lambda^2 \boldsymbol{\tau} , \quad (26)$$

where λ^2 represents the Lagrange multiplier. The magnitude bound of the output moment vector can be obtained from Eq. (26) as follows:

$$\lambda_{min} \leq \frac{\|\boldsymbol{m}\|}{\|\boldsymbol{\tau}\|} \leq \lambda_{max} , \quad (27)$$

where λ_{min} and λ_{max} are the square roots of the minimum and maximum eigenvalues of $J_q^{-1} J_x J_x^T J_q^{-1}$. From Eq. (27), the index of the moment transmissibility can be defined as

$$I = \frac{\lambda_{max}}{\lambda_{min}} . \quad (28)$$

The index I is greater than or equal to 1. When I is equal to 1, the SPM has the best moment transmissibility; as the index becomes large, the SPM becomes closer to singular. The system is said to have good transmissibility when the transmissibility index is less than $1.43(\approx 1/0.7)$ in general [26]. By utilizing this index, the optimal design problem of SPM can be formulated as

$$minimize \quad \int_W I \, dW, \quad (29)$$

$$subject \ to \ \ \alpha_{min} \leq \alpha \leq \alpha_{max}, \quad \beta_{min} \leq \beta \leq \beta_{max},$$

$$\eta_{min} \leq \eta \leq \eta_{max} ,$$

where W is the target workspace of SPM, and the design variables α, β, and η represent the angular lengths of the first, second, and ground links, respectively.

D. User Interface

The targeted stimulation point and orientation of the line of stimulation is determined through the developed image-guided graphical user interface (Fig. 5). This user-friendly interface
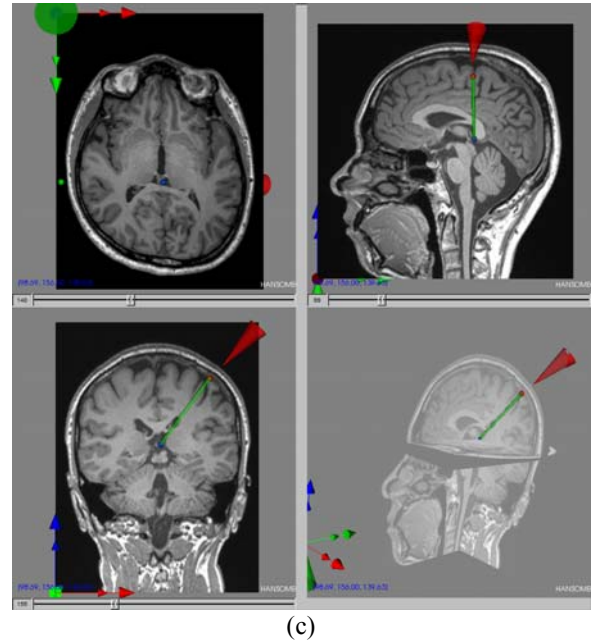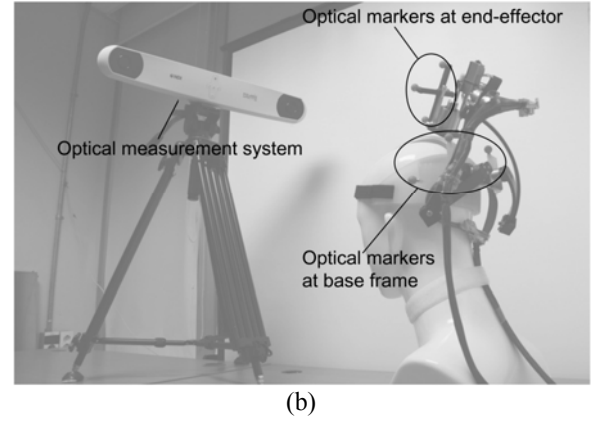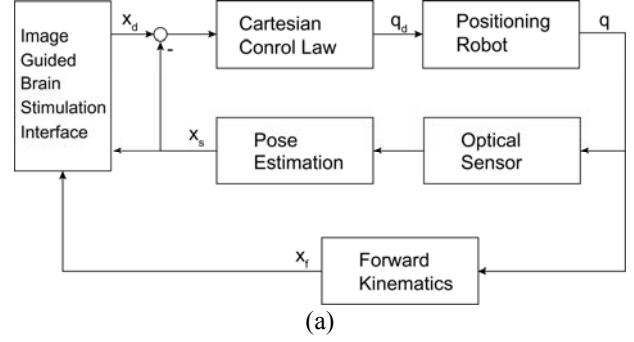

(a)

(b)

(c)

Figure 5. (a) Overall control architecture, (b) optical tracking system and (c) graphical user interface of image-guided brain stimulation.

(a)   (b)
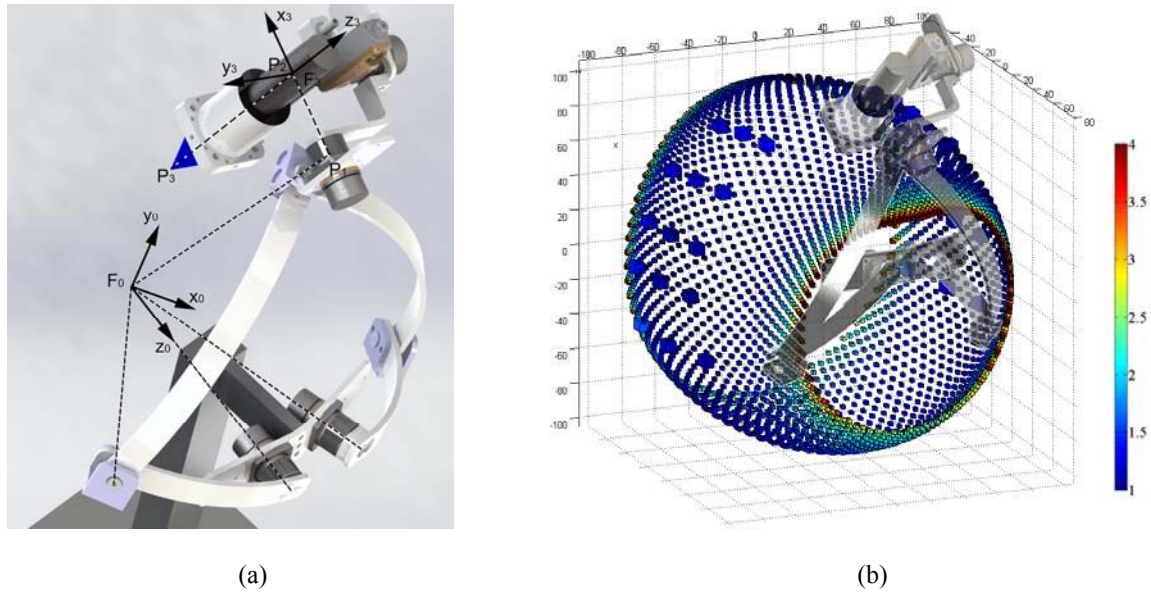
Figure 6. (a) Final design of the wearable robotic positioning system and (b) workspace and its moment transmissibility with optimized link parameters.

not only shows the current posture of the device during navigation but also acts as an input terminal for user control commands. The desired stimulation posture defined in Cartesian space $\mathbf{x}_d$ by this graphical interface is converted into joint variables $\mathbf{q}_d$ through inverse kinematics (III.B), and then delivered to the robot controller for low-level joint control. At the same time, the current posture of the ultrasound transducer $\mathbf{x}$ is periodically updated using both forward kinematics (III.A) with current robot joint angles $\mathbf{q}$ and an optical tracking system with infrared reflective markers (Fig. 5(b)). Fig. 5(c) shows a snapshot of the developed image-guided user interface. The image registration and navigation in the software were developed using an open source component-based framework, IGSTK (Image-Guided Surgery Toolkit) [29]. Four grayscale images in the interface are magnetic resonance imaging (MRI) images of a subject in different planes. The subject-specific imaging data was obtained prior to the experiment to take each subject's anatomical brain differences into account. The small red sphere on the MRI images represents the desired

TABLE I
OPTIMIZED DESIGN VALUES OF SPHERICAL PARALLEL MECHANISM

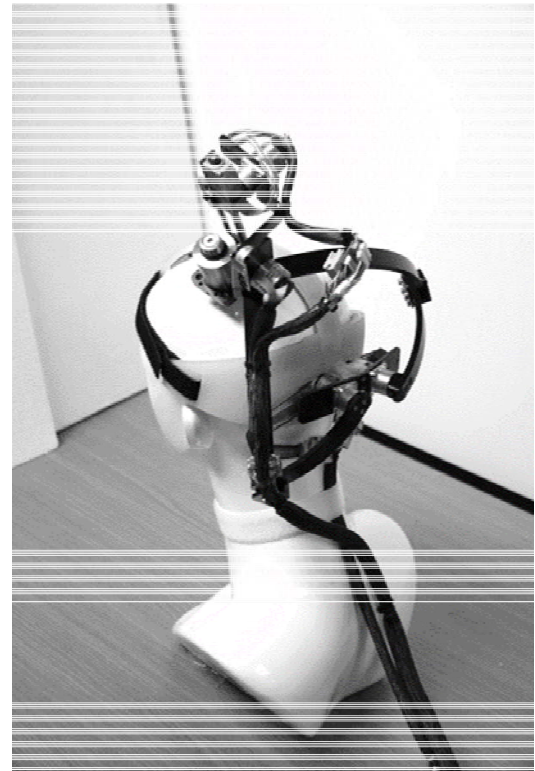| Linkage parameters	Design value
α, δ	42°
β, γ	80°
η	20°

Figure 7. Final prototype. The robotic positioning system consists of a two-DOF spherical five-bar parallel linkage and a three-DOF serial linkage, enabling five-DOF positioning and orientation of the transducer. Head-fixing parts with Velcro straps were also fabricated with a 3D printer based on 3D data of the patient model.

stimulation point, and the thin green line defined by both the red sphere and the blue sphere is the line of ultrasound stimulation. The red cone represents the current ultrasound beaming from the attached end effector (a focused ultrasound transducer) when it is turned on. The desired stimulation point is then going to be stimulated by the ultrasound. Depending on the operator's choice, it can be the centroid of the ultrasound focal zone, far or near edge of the focus. Graphic user interface supported by the developed automatic robotic system can make various tedious tasks by the operators done easily and accurately. For example, the normal incident angle leading to the highest ultrasound transmission can be automatically achieved by the system through simple image processing.

E. Open-loop Positioning and Closed-loop Positioning

Open-loop positioning locates the end-effector of the robot to a given desired pose only with its joint feedback while closed-loop positioning uses the final error at the end-effector measured by an optical measurement system as well as joint information in order to locate the end-effector to a desired pose.

First, we performed open-loop positioning to evaluate the inverse kinematic control. Four desired positions that are sparsely located in the right and left brain were chosen for the task. All of the points are in primary somatosensory region of the brain. The desired orientation of these positions was set to point in the direction to the center of SPM. A trapezoidal trajectory connecting these four desired orientations was planned beforehand, as shown in Fig. 8(a). Experiments were performed 25 times.

The end-effector pose can be estimated by forward kinematics using joint information, and then, the error between the desired one and the estimated one can be estimated. However, more error in the real is expected to exist than the estimated error due to various error sources such as kinematic robot modeling error, registration error, and unstable base attachment. To address this problem, a closed-loop positioning was implemented. We define the position error as the distance between the desired position and the actual position of focal point of ultrasound which is estimated from the position of the end effector. The error is measured by an optical measurement system having the accuracy of ~0.25 mm. Similarly, the orientation error is defined as the angle between the desired vector and the actual final vector measured by this optical system. We implemented a feedback closed-loop control using the optical measurement system [30]. The pose error is feedbacked to the controller to produce new desired control output; The joint desired joint angle q_d is calculated by

$$q_d = KJ^{-1}\Delta x + q \tag{30}$$

where J is the robot Jacobian matrix, K is a gain matrix, q is current joint angle, and Δx is the measured pose error.
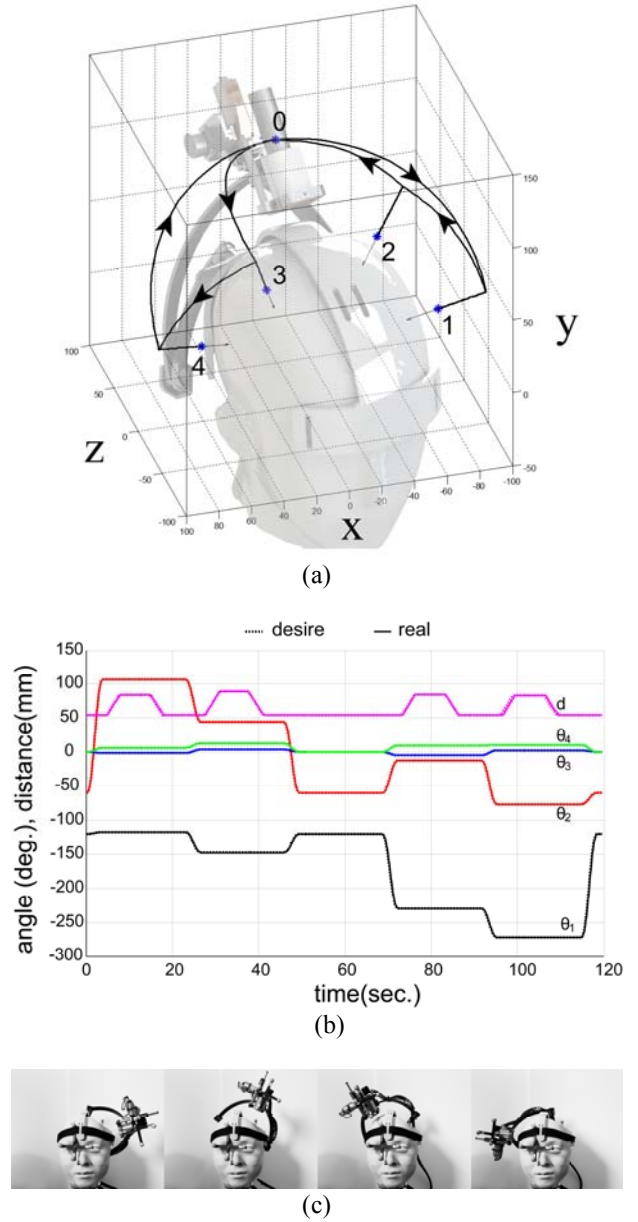

(a)

(b)

(c)

Figure 8. A trajectory tracking experimental result. For a given trajectory (a), the trajectory tracking results are shown with a plot (b) and snapshots (c). The plot shows the desired and the real joint values.

IV. RESULTS

A. Prototype

The optimization problem given in Eq. (29) was performed numerically. As a result, the variables α, β, δ, γ, and η that determine the lengths of SPM linkages were obtained. Table I summarizes the obtained optimized linkage parameters. As mentioned above, α and δ, and β and γ were kept the same to make the linkage symmetric. The transmissibility index is less than 1.25 (=1/0.8) was set as a desired target value and this was met in the workspace as shown in Fig. 6(b).

Fig. 6(a) shows the final design using the resultant linkage parameters. Fig. 6(b) presents the final workspace of the optimized SPM; it also shows the moment transmissibility of the mechanism. The workspace is shown with sampling points depicted by colorized cubes. The color indicates the moment transmissibility at the point. Values closer to 1 (corresponding to blue) represent better transmissibility. As shown in Fig. 6(b), the final workspace includes the initial target workspace with a sufficiently large margin. The large cubes here represent the initial target workspace, as shown in Fig. 2. Note that all of the transmissibility indices of the points on the target workspace are near to one. From this analysis, we conclude that the final design meets the requirements of the target workspace. Moreover, this design can efficiently transmit the input torques to the end-effector in the target workspace. Head-fixing parts with Velcro straps were also fabricated using a 3D printer, based on the shape data of the patient model. The total weight of the robotic system was measured at 710 g. Fig. 7 shows the final prototype of the automatic positioning device.

B. Positioning experiments

The developed system was tested with a positioning task. Figure 8(b and c) shows the result of an open-loop trajectory tracking experiment. The solid lines indicate the desired joint trajectories; the dotted lines are the real trajectories. The experimental result represents good joint tracking performance showing little tracking errors for almost all of the trajectories.

In the so-called open-loop control in Fig. 8, the measurement of the error in the end-effector revealed that the position errors are 6.3 mm and the orientation errors 6.9 degree on average at the four desired poses due to various error sources mentioned before. In the error analysis, the size and the location of ultrasound focus and the effect of distortion by skull are not considered. Only the mechanical positioning function is evaluated in the error analysis.

Then, a closed-loop positioning control was applied by using an optical tracking system. With feedback of the error, the final position error reduces from 6.3 mm to 0.1 mm and the orientation error from 6.9 deg. to less than 0.1 degree on average (Fig. 9).

Manual positioning is also evaluated as a comparison study (Fig. 9). In manual positioning task, users position the ultrasound transducer with a commercial fixing arm by looking at the real-time errors in our navigation software. Experiments showed that the errors of manual positioning at the same four desired pose were 7.1 mm in position and 6.0 degree in orientation on average when time constraint (~ 1min) was given. Without time constraint, the average error decreased to 4.3 mm in position and 5.5 degree in orientation. Although users can read and see the errors graphically in real time, it turned out that reducing errors less than 5.0 mm in position and 5.0 degree in orientation at the same time is quite challenging and difficult because all errors should be adjusted altogether. The result proves that automatic robotic positioning with visual feedback is not only convenient but also makes the positioning far more accurate (Fig. 9).
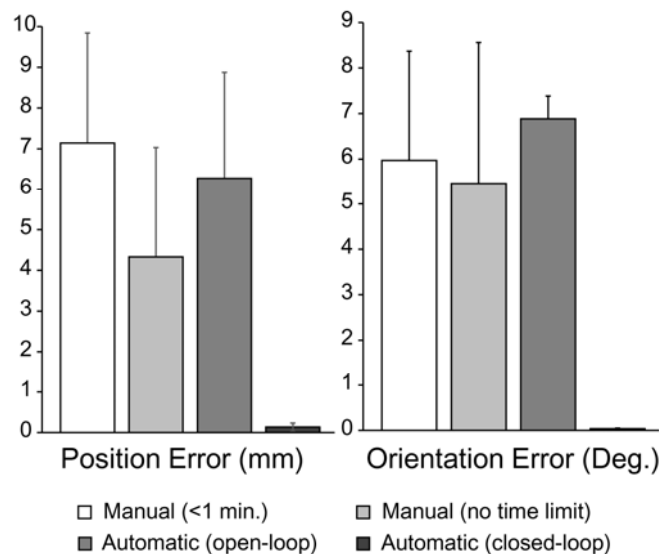

Figure 9. Comparison of errors: manual positioning, open-loop control positioning with only joint angle feedback, and closed-loop control positioning with a real-time optical tracking of end-effector pose.

V. CONCLUSION

Ultrasound is expected to play an important role as a novel modality for noninvasive brain stimulation because of its improved spatial resolution and penetration capability compared with the existing modalities. In this study, we proposed a wearable robotic system for automatic transducer positioning. The robotic device has a total five DOF, sufficient for arbitrary positioning over human heads with an arbitrary orientation. For optimized design, we proposed a combined parallel-and-serial linkage mechanism, and a link-parameter optimization method for the given workspace. Simulation and experimental results show the proposed mechanism has good torque transmissibility over the entire workspace and tracking and positioning performance is sufficiently good for ultrasound positioning.

Finally, we are going to do human brain stimulation using this device to study the ultrasound effect on the activity of the primary somatosensory region. We are currently preparing for clinical trial and are working on optimizations of the combined apparatus. For example, a water bag is being introduced to acoustically couple the ultrasound transducer to the scalp. The material and design for this bag are being optimized to minimize resistive contact force to prevent a loss in attachment stability.

REFERENCES

[1] F. Fregni and A. Pascual-Leone, "Technology insight: Noninvasive brain stimulation in neurology-perspectives on the therapeutic potential of rTMS and tDCS," *Nat. Clin. Pract. Neurol.,* vol. 3, pp. 383-93, Jul. 2007.

[2] W. Legon, T. F. Sato, A. Opitz, J. Mueller, A. Barbour, A. Williams and W. J. Tyler, "Transcranial focused ultrasound modulates the activity of primary somatosensory cortex in humans," *Nat. Neurosci.,* vol. 17, pp. 322-9, Feb. 2014.

[3] J. Mueller, W. Legon, A. Opitz, T. F. Sato, and W. J. Tyler, "Transcranial focused ultrasound modulates intrinsic and evoked EEG dynamics," *Brain. Stimul.*, vol. 7, pp. 900-8, Nov-Dec 2014.

[4] W. Lee, H. Kim, Y. Jung, I. U. Song, Y. A. Chung, and S. S. Yoo, "Image-guided transcranial focused ultrasound stimulates human primary somatosensory cortex," *Sci. Rep.,* vol. 5, p. 8743, 2015.

[5] Y. Tufail, A. Matyushov, N. Baldwin, M. L. Tauchmann, J. Georges, A. Yoshihiro, S. I. Tillery, and W. J. Tyler, "Transcranial pulsed ultrasound stimulates intact brain circuits," *Neuron,* vol. 66, pp. 681-94, Jun. 2010.

[6] R. L. King, J. R. Brown, W. T. Newsome, and K. B. Pauly, "Effective parameters for ultrasound-induced in vivo neurostimulation," *Ultrasound Med. Biol.,* vol. 39, pp. 312-31, Feb. 2013.

[7] E. Mehic, J. M. Xu, C. J. Caler, N. K. Coulson, C. T. Moritz, and P. D. Mourad, "Increased anatomical specificity of neuromodulation via modulated focused ultrasound," *PLoS One,* vol. 9, p. e86939, 2014.

[8] W. J. Tyler, Y. Tufail, M. Finsterwald, M. L. Tauchmann, E. J. Olson, and C. Majestic, "Remote excitation of neuronal circuits using low-intensity, low-frequency ultrasound," *PLoS One,* vol. 3, p. e3511, 2008.

[9] S. Hameroff, M. Trakas, C. Duffield, E. Annabi, M. B. Gerace, P. Boyle, A. Lucas, Q. Amos, A. Buadu, and J. J. Badal, "Transcranial ultrasound (TUS) effects on mental states: a pilot study," *Brain Stimul.,* vol. 6, pp. 409-15, May 2013.

[10] F. J. Fry, H. W. Ades, and W. J. Fry, "Production of reversible changes in the central nervous system by ultrasound," *Science,* vol. 127, pp. 83-4, Jan. 1958.

[11] R. T. Mihran, F. S. Barnes, and H. Wachtel, "Temporally-specific modification of myelinated axon excitability in vitro following a single ultrasound pulse," *Ultrasound Med. Biol.,* vol. 16, pp. 297-309, 1990.

[12] E. P. Chronicle, A. J. Pearson, and C. Matthews, "Development and positioning reliability of a TMS coil holder for headache research," *Headache,* vol. 45, pp. 37-41, Jan. 2005.

[13] L. Richter, P. Trillenberg, A. Schweikard, and A. Schlaefer, "Stimulus intensity for hand held and robotic transcranial magnetic stimulation," *Brain Stimul.,* vol. 6, pp. 315-21, May 2013.

[14] L. Zorn, P. Renaud, B. Bayle, L. Goffin, C. Lebosse, M. de Mathelin, and J. Foucher, "Design and evaluation of a robotic system for transcranial magnetic stimulation," *IEEE Trans. Biomed. Eng.,* vol. 59, pp. 805-15, Mar. 2012.

[15] P. Abolmaesumi, S. E. Salcudean, Z. Wen-Hong, M. R. Sirouspour, and S. P. Dimaio, "Image-guided control of a robot for medical ultrasound," *IEEE Trans. Robot. Autom.,* vol. 18, pp. 11-23, 2002.

[16] D. Stoianovici, C. Kim, F. Schafer, C. M. Huang, Y. Zuo, D. Petrisor, and M. Han, "Endocavity Ultrasound Probe Manipulators," *IEEE/ASME Trans. Mechatronics.,* vol. 18, pp. 914-921, Jun 2013.

[17] C. Poquet, P. Mozer, M. A. Vitrani, and G. Morel, "An Endorectal Ultrasound Probe Comanipulator With Hybrid Actuation Combining Brakes and Motors," *IEEE/ASME Trans. Mechatronics.,* vol. 20, pp. 186-196, 2015.

[18] S. Yang, R. A. MacLachlan, and C. N. Riviere, "Manipulator design and operation for a six-degree-of-freedom handheld tremor-canceling microsurgical instrument," *IEEE/ASME Trans. Mechatronics.,* vol. 20, pp. 761-72, Apr. 2015.

[19] P. K. Jamwal, S. Q. Xie, S. Hussain, and J. G. Parsons, "An adaptive wearable parallel robot for the treatment of ankle injuries," *IEEE/ASME Trans. Mechatronics.*, vol. 19, pp. 64-75, 2014.

[20] R. Martuzzi, W. van der Zwaag, J. Farthouat, R. Gruetter, and O. Blanke, "Human finger somatotopy in areas 3b, 1, and 2: a 7T fMRI study using a natural stimulus," *Hum. Brain Mapp.,* vol. 35, pp. 213-26, Jan 2014.

[21] K. Hynynen, G. T. Clement, N. McDannold, N. Vykhodtseva, R. King, P. J. White, S. Vitek, and F. A. Jolesz, "500-element ultrasound phased array system for noninvasive focal surgery of the brain: a preliminary rabbit study with ex vivo human skulls," *Magn. Reson. Med.*, vol. 52, pp. 100-7, Jul 2004.

[22] M. F. Bear, B. W. Connors, M. A. Paradiso, "Chapter 12, The somatic sensory system," in *Neuroscience: Exploring the Brain*, 3rd ed., Lippincott Williams and Wilkins, 2006, pp. 387-422.

[23] Korean Agency for Technology and Standard. (2010), 3D Shape Measurement Data. Available at: http://sizekorea.kats.go.kr/

[24] T. K. Tanev, "Kinematics of a hybrid (paralle-serial) robot manipulator," *Mech. Mach. Theory*, vol. 35, pp. 1183-96, Sep 2000.

[25] L. W. Tsai and S. Joshi, "Kinematic analysis of 3-DOF position mechanisms for use in hybrid kinematic machines," *J. Mech. Design*, vol. 124, pp.245-53, 2002.

[26] C. Wu. X. J. Liu. L. Wang, and J. Wang, "Optimal design of spherical 5R parallel manipulators considering the motion/force transmissibility," *J. Mech. Design*, vol. 132, pp. 0310021-10, Mar. 2010.

[27] M. Ouerfelli and V. Kumar, "Optimization of a spherical five-bar parallel drive linakge," *J. Mech. Design*, vol. 116, pp. 166-73, Mar. 1994.

[28] L. W. Tsai, *Robot Analysis: The mechanics of serial and parallel manipulators*. Wiley, New York, 1999.

[29] A. Enquobahrie, P. Cheng, K. Gary, L. Ibanez, D. Gobbi, F. Lindseth, Z. Yaniv, S. Aylward, J. Jomier, and K. Cleary, "The image-guided surgery toolkit IGSTK: an open source C++ software toolkit," *J. Digit. Imaging,* vol. 20 Suppl 1, pp. 21-33, Nov 2007.

[30] S. Lee, Y. Nakamura, K. Yamane, T. Toujo, S. Takahashi, Y. Tanikawa, and H. Takahashi, "Image Stabilization for In Vivo Microscopy by High-Speed Visual Feedback Control," *IEEE Trans. Robot.,* vol. 24, pp. 45-54, Feb. 2008.

Junwoo Kim received his B.S. degree in natural science from Yonsei University, Seoul, Republic of Korea in 2001 and his Ph.D. degree in mechanical engineering from the same university in 2013.

From 2013 to 2015, he was a Postdoctoral Research Fellow at the Center for Robotics Research at the Korea Institute of Science and Technology, Republic of Korea. Since 2015, he has been a Research Specialist with Korea Polar Research Institute, Incheon, Republic of Korea. His research interests lie in the fields of mechanism synthesis, robotics, vibratory systems, and polar engineering.
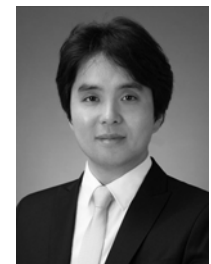
Sungon Lee received his B.S. degree in mechanical design and product engineering from Seoul National University, Seoul, Republic of Korea, in 1997; his M.S. degree in mechanical engineering from POSTECH, Pohang, Republic of Korea, in 1999; and his Ph.D. degree in mechano-informatics from the University of Tokyo, Japan, in 2008.

From 2010 to 2012, he was a Postdoctoral Research Fellow with the Center for Systems Biology, Massachusetts General Hospital, Harvard Medical School, Boston, MA, USA. From 1999 to 2015, he was a Senior Research Scientist with the Korea Institute of Science and Technology, Republic of Korea. Since 2015, he has been an Assistant Professor at the school of electrical engineering, Hanyang University, Ansan, Republic of Korea. His research interests include biomedical robotics, surgical robots, medical image processing, and motion compensation systems.